Journal of Engineering Science and Technology
Vol. 20, No. 6 (2025) 2064 - 2084

METAHEURISTIC OPTIMIZATION OF PEROVSKITE SOLAR CELL PERFORMANCE USING TAGUCHI GREY RELATIONAL ANALYSIS WITH GREY WOLF OPTIMIZER

K. E. KAHARUDIN[2], F. SALEHUDDIN[1,*],
S. A. M. JUNOS[1], NABILAH A. JALALUDIN[1],
N. FARINA. M. NAZLI[1], F. ARITH[1], A. S. M. ZAIN[1], N. R. M. RAFIDI[2]

[1]Micro and Nano Electronics (MiNE), CeTRI, Faculty of Electronics and Computer Technology and Engineering, Universiti Teknikal Malaysia Melaka, Hang Tuah Jaya, Durian Tunggal, 76100 Melaka
[2]School of Engineering and Built Environment, Lincoln University College, No. 2, Jalan Stadium, SS 7/15, Kelana Jaya, 47301, Petaling Jaya, Selangor, Darul Ehsan, Malaysia
*Corresponding Author: fauziyah@utem.edu.my

Abstract

Perovskite solar cells offer numerous benefits like simplified production, adaptability, and affordability in contrast to silicon-based counterparts. Yet, enhancing their power conversion efficiency remains difficult due to the diverse effects of various layer parameters variability. This research work proposes the utilization of metaheuristic approach in optimizing multiple layer parameters of Perovskite Solar Cell (PSC) for better output properties. The metaheuristic approach sequentially employs the L_{27} orthogonal array (OA) Taguchi-based design of experiment (DoE), Grey Relational Analysis (GRA), Multiple Linear Regression (MLR) and Grey Wolf Optimizer (GWO). The L_{27} OA Taguchi-based DoE is initially employed to mine sufficient output data simulated using one dimensional solar cell capacitance simulator (SCAPS-1D). GRA is utilized to merge the J_{sc} and *PCE* into a single representative grade called Grey Relational Grade (GRG) for holistically improved PSC performances. MLR is then performed to establish the linear relationship between layer parameters and the computed GRGs, thereby modeling the objective function. The best solutions of the MLR model are finally predicted by using GWO algorithm where both J_{sc} and *PCE* are successfully optimized to 25.67 mA/cm^2 and 24.73%, respectively.

Keywords: Grey relational analysis, Grey wolf optimizer, Power conversion efficiency, Short circuit current density, Taguchi.

1. Introduction

Currently, the global need for energy relies significantly on fossil fuels. Nevertheless, this finite reserve of fossil fuels is on the brink of exhaustion. Furthermore, it poses environmental hazards due to its emission of greenhouse gases. Thus, in the absence of exploration into alternative or renewable sources, the world is poised to encounter a grave energy predicament in the foreseeable future. Renewable energies represent a pure form of energy, emitting no hazardous substances towards environments. Amid the spectrum of renewable energy choices, solar energy emerges as the swiftest expanding resource owing to its simple adoption. Solar panels, often known as PV cells or photovoltaic cells, directly convert sunlight into electrical power. Thin-film solar cells, distinct from conventional photovoltaic cells, employ a thin semiconductor layer, like perovskite-based absorbers, making them flexible and lightweight, and consequently more cost-effective than silicon solar cells [1].

Numerous researchers have rigorously attempted to attain the exceptional photovoltaic efficiency of perovskite solar cells (PSCs) utilizing the $CH_3NH_3PbI_3$ absorber material [2-5]. Nevertheless, a fundamental hurdle to their extensive commercial deployment lies in the stability issue confronting perovskite solar cells (PSCs), necessitating resolution. Researchers have put forward various techniques to enhance both the power conversion efficiency (PCE) and stability of PSCs. Dimensionality and parameter optimization involve the utilization of a stable organic cation during perovskite material formation, while interface engineering stands as a pivotal strategy in enhancing both stability and efficiency.

In recent times, several optimization approaches have been employed to discover the most effective blend of material parameters for solar cells, resulting in superior electrical and optical performance. Analysis of MAPbI3-based perovskite solar cells (PSCs) was conducted by combining machine learning (ML) models with SCAPS-1D simulations [6]. XGBoost ML algorithm achieved the highest accuracy in predicting PCE in which the optimal structure reached a PCE of 34.65%. Additionally, an ANN-based ML model accurately predicted PCE ($R^2 \approx 0.999$) using five semiconductor parameters of thin-film solar cells (TFSCs) [7]. The best configuration achieved a PCE of 30.18%. Real Coded Genetic Algorithm (RCGA) was integrated with MATLAB and Atlas Silvaco for multi-dimensional optimization [8].

The proposed method closely matched experimental results and outperformed conventional techniques, achieving a solar cell PCE of 26.08% under AM1.5 conditions. Employing response surface methodology (RSM), researchers crafted and optimized nanocrystalline transparent coatings for Si solar cells. The outcome was reflection values below 5% across a wide spectrum of wavelengths, with minimal reflection recorded at 560 nm for a ZnO nanoparticle size of 38 nm, suggesting significant advancements in photo-activity [9]. The utilization of RSM for optimization purposes in an organic tandem solar cell has yielded a significant 47.7% increase in PCE, driven by modifications in the thicknesses of the front and back cells [10].

Apart from that, the utilization of the Taguchi approach in estimating the optimal thickness of cadmium sulfide (CdS), perovskite ($CH_3NH_3PbI_3$), and copper telluride (CuTe) yielded elevated overall PSC performances [11]. The utilization of the Taguchi method also extended to the fabrication of photoanodes for dye-sensitized solar cells (DSSC), showcasing a significant improvement in FF and PCE [12]. Using the Taguchi technique, the optimal bandgap combination for the

CIGS solar cell was established, resulting in enhanced photovoltaic performance, achieving an average efficiency of 22.08% [13]. Moreover, metaheuristic algorithms such as the bald eagle search and genetic algorithm were applied to determine the optimal parametric configuration of solar cells [14-18]. These algorithms have shown promise in forecasting the ideal material parameters for enhanced solar cell efficiency.

In the quest to improve electrical performances, solar cell simulation can be merged with multiple optimization techniques [19-21]. These methodologies offer predictive insights into device performance prior to real-world testing and manufacturing, thus offering substantial time and cost savings. This research introduces an approach that combines SCAPS-1D simulation with a hybrid optimization strategy involving L27 Taguchi Grey relational analysis (GRA), multiple linear regression (MLR), and Grey wolf optimizer (GWO) algorithm to optimize perovskite solar cell layer parameters for enhanced J_{sc} and PCE.

Significant elements in enhancing the optimization strategy for the perovskite solar cell include developing a novel hybrid optimization method that incorporates L27 Taguchi-GRA, multiple linear regression (MLR), and Grey wolf optimizer (GWO) algorithm; determining the most significant layer parameters impacting J_{sc} and PCE; forecasting the optimal combination of layer parameters for achieving maximum J_{sc} and PCE; validating the proposed metaheuristic approach by comparing it with pre-metaheuristic outputs.

2. Simulation and Metaheuristic Optimization

The simulation work performed in this recent study was referenced from the work of Kohnehpoushi et al. [22] and Sobayel et al. [23] in which both hole and electron transport layer of the PSC device employed molybdenum disulfide (MoS2) and tungsten disulfide (WS2) material respectively. SCAPS-1D software invented by Department of Electronics and Information Systems University of Gent Belgium [24] was utilized to perform numerical simulation of the PSC device. The modelling of the PSC device was assisted by the proposed metaheuristic approach involving L_{27} Grey Relational Grade (GRG), Multiple Linear Regression (MLR) and Grey Wolf Optimizer (GWO) algorithm which will be further explained in the following sections.

2.1. PSC device simulation

The PSC device was initially developed and simulated with multiple stacked layers as depicted in Fig. 1. The SCAPS-1D simulation essentially solved three semiconductors equations: Poisson, hole continuity and electron continuity. The impact of multiple layer thickness and doping concentration for each material was hypothetically investigated in order to outline their ideal magnitudes as the PSC device mechanism was explored in term of efficacy and stability especially in ambient conditions. In this work, $CH_3NH_3PbI_3$ perovskite was utilized as an absorber layer sandwiched between MoS_2 and WS_2 as hole transport layer (HTL) and electron transport layer (ETL) respectively.

Spray Pyrolyzed Fluorine-Doped Tin Oxide (SnO_2:F) was utilized as transparent conducting oxide (TCO) layer that acted as a medium for low resistance's contacts without having to block the sunlight. The illumination for this simulation employed a standard AM1.5G spectrum (1000 W/m^2) at

temperature of 300 K. Metal work function (WF) for both front and back contacts of the PSC device were tuned at 4.4 eV and 5.1 eV respectively. The initial layer parameters for each material type utilized in the numerical study are supported by previous literature studies [25-28] as summarized in Table 1 in which χ, E_r, E_g, μ_n, μ_p, N_v, N_c, Na, N_d and N_t represents electron affinity, relative permittivity, bandgap energy, electron mobility, hole mobility, effective valence band density, effective conduction band density, acceptor density, donor density and defect density respectively.

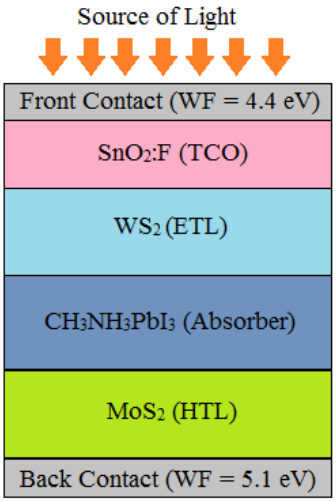

Fig. 1. Multiple Stacked Layers of the PSC device.

Table 1. Simulation parameters for multiple layers of materials.

Parameters	SnO_2:F (TCO)	WS_2 (ETL)	$CH_3NH_3PbI_3$ (Absorber)	MoS_2 (HTL)
Thickness (µm)	0.2	0.2	0.2	0.2
χ (eV)	4	3.95	3.9	4.2
E_r	9	13.6	6.5	3
E_g (eV)	3.5	1.8	1.55	1.29
μ_n (cm^2/Vs)	20	100	2	100
μ_p (cm^2/Vs)	10	100	2	150
N_v (cm^{-3})	1.8×10^{19}	1×10^{19}	1.8×10^{19}	1.8×10^{19}
N_c (cm^{-3})	2.2×10^{18}	1×10^{19}	2.2×10^{18}	2.2×10^{18}
N_a (cm^{-3})	-	-	-	1×10^{17}
N_d (cm^{-3})	1×10^{18}	1×10^{18}	1×10^{13}	-
N_t (cm^{-3})	1×10^{15}	1×10^{15}	2.5×10^{13}	1×10^{14}

2.2. Metaheuristic optimization

In mathematical optimization, a metaheuristic is defined as a higher level process to form, generate, or opt partial search algorithm that may recommend an acceptably decent solution to a specific optimization problem. In this work, a combined set of statistical method and machine learning is proposed to form a

metaheuristic approach in modelling multiple layer parameters of the PSC device for sufficiently better output performances. Figure 2 depicts the proposed flowchart of the metaheuristic modelling of the PSC device involving L_{27} Grey Relational Analysis (GRA), Multiple Linear Regression (MLR) and Grey Wolf Optimizer (GWO) algorithm. Taguchi OA is a fractional design based on a design matrix proposed by Dr. Genichi Taguchi, commonly used for consideration of a selected subset of combined multiple inputs at multiple levels.

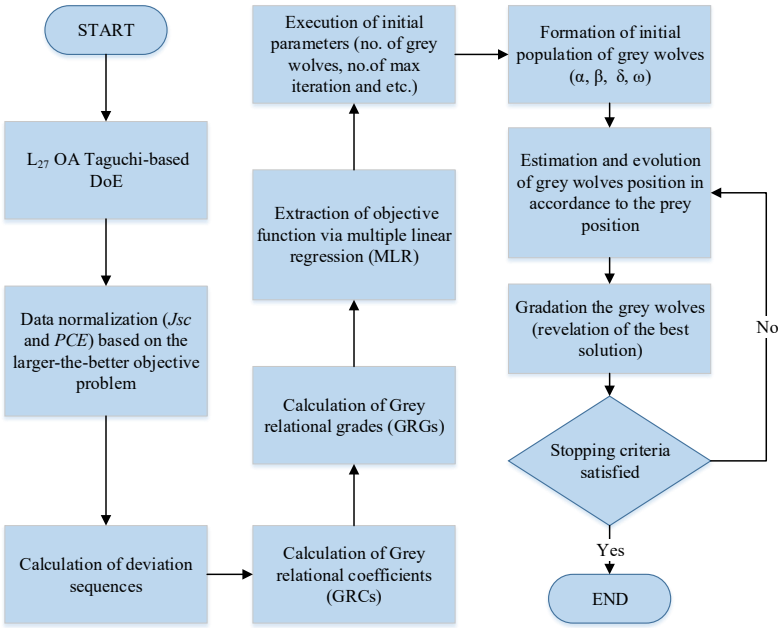

Fig. 2. Proposed flowchart of the metaheuristic modelling of the PSC device.

In this work, the L_{27} OA Taguchi-based DoE is employed in order to utilize multiple combinations of layer parameters in attaining 27 variations of J_{sc} and *PCE* of the PSC device. The layer parameters of the PSC device are varied into low level, medium level and high level as listed in Table 2.

Table 2. Levels of layer parameters.

Sym.	Layer Parameters	Units	Level		
			Low	Medium	High
a	SnO_2:F thickness	μm	0.2	0.5	0.8
b	SnO_2:F donor density	$(\times 10^{18})$ cm^{-3}	1	5	9
c	WS_2 thickness	μm	0.2	0.5	0.8
d	WS_2 donor density	$(\times 10^{18})$ cm^{-3}	1	5	9
e	$CH_3NH_3PbI_3$ thickness	μm	0.2	0.5	0.8
f	$CH_3NH_3PbI_3$ donor density	$(\times 10^{13})$ cm^{-3}	1	5	9
g	MoS_2 thickness	μm	0.2	0.5	0.8
h	MoS_2 acceptor density	$(\times 10^{17})$ cm^{-3}	1	5	9

The magnitudes of J_{sc} and *PCE* for each row are simulated and recorded accordingly in Table 3. To simplify the optimization process, the Grey relational analysis (GRA) is employed in which the magnitudes of both J_{sc} and *PCE* are manipulated by merging them into a single representative unit called Grey relational grade (GRG). The GRA is originally developed by Professor Julong Deng [29] from Huazhong University of Science and Technology, commonly utilized to solve uncertainty in data or information.

Table 3. L_{27} Taguchi-based DoE and the corresponding magnitudes.

Exp. no.	*a*	*b*	*c*	*d*	*e*	*f*	*g*	*h*	J_{sc} (mA/cm^2)	*PCE* (%)
1	0.2	1	0.2	1	0.2	1	0.2	1	21.21	19.38
2	0.2	1	0.2	1	0.5	5	0.5	5	24.65	23.60
3	0.2	1	0.2	1	0.8	9	0.8	9	25.64	24.72
4	0.2	5	0.5	5	0.2	1	0.2	5	22.1	21.02
5	0.2	5	0.5	5	0.5	5	0.5	9	24.73	23.90
6	0.2	5	0.5	5	0.8	9	0.8	1	25.6	23.99
7	0.2	9	0.8	9	0.2	1	0.2	9	22.23	21.38
8	0.2	9	0.8	9	0.5	5	0.5	1	24.63	23.04
9	0.2	9	0.8	9	0.8	9	0.8	5	25.49	24.43
10	0.5	1	0.5	9	0.2	5	0.8	1	22.2	20.18
11	0.5	1	0.5	9	0.5	9	0.2	5	24.62	23.58
12	0.5	1	0.5	9	0.8	1	0.5	9	25.5	24.60
13	0.5	5	0.8	1	0.2	5	0.8	5	22.14	21.07
14	0.5	5	0.8	1	0.5	9	0.2	9	24.55	23.07
15	0.5	5	0.8	1	0.8	1	0.5	1	25.39	23.80
16	0.5	9	0.2	5	0.2	5	0.8	9	21.13	20.24
17	0.5	9	0.2	5	0.5	9	0.2	1	24.55	22.93
18	0.5	9	0.2	5	0.8	1	0.5	5	25.55	24.48
19	0.8	1	0.8	5	0.2	9	0.5	1	22.16	20.27
20	0.8	1	0.8	5	0.5	1	0.8	5	24.49	23.46
21	0.8	1	0.8	5	0.8	5	0.2	9	25.34	24.44
22	0.8	5	0.2	9	0.2	9	0.5	5	87.78	19.96
23	0.8	5	0.2	9	0.5	1	0.8	9	24.52	23.68
24	0.8	5	0.2	9	0.8	5	0.2	1	25.49	23.88
25	0.8	9	0.5	1	0.2	9	0.5	9	21.96	21.10
26	0.8	9	0.5	1	0.5	1	0.8	1	24.57	22.97
27	0.8	9	0.5	1	0.8	5	0.2	5	25.46	24.39

Basically, the primary aim of the optimization was to find the optimal layer parameters that may generate larger J_{sc} and *PCE* of the PSC device. For that reason, the magnitudes of both J_{sc} and *PCE* need to be normalized with respect to their corresponding problem which is larger-the-better. The mathematical formulation for normalizing larger-the-better objective problem is given as follows:

$$Z_o^{\wedge} = \frac{Z_o(n) - minZ_o(n)}{maxZ_o(n) - minZ_o(n)} \quad (1)$$

where $Z_o(n)$, min $Z_o(n)$ and max $Z_o(n)$ represent the output parameters of the PSC device (J_{sc} and *PCE*), the minimum magnitude of the output parameter in a column and the maximum magnitude of the output parameter in a column respectively.

Subsequently, the deviation sequence, $\Delta_o(n)$ for each row is calculated by subtracting the reference value from the normalized magnitude of each corresponding row as follows:

$$\Delta_o(n) = |Z_r^*(n) - Z_o^{\wedge}(n)| \quad (2)$$

where $Z_r^*(n)$ is the reference value which is commonly set to 1 (unity). The calculated $\Delta_o(n)$ for every row is then used to compute the Grey relational coefficient (GRC) as follows:

$$GRC(n) = \frac{\Delta_{min} + \varepsilon\Delta_{max}}{\Delta_o(n) + \varepsilon\Delta_{max}} \quad (3)$$

where ε stands for the distinguishing coefficient that commonly ranged from 0 to 1. For this case, the magnitude of ε is preferred to be 0.5 because it does contribute moderate distinguishing impact and stability in which the calculated GRC and overall rank of grades will not much affected. The Δ_{max} and Δ_{min} stand for maximum and minimum magnitude of the deviation for each column respectively. The computed GRC of each row is then divided with the total output parameters (two) as mathematically formulated as:

$$GRG(n) = \frac{1}{2}\left[GRC_{Jsc}(n) + GRC_{PCE}(n)\right] \quad (4)$$

Extensively, the importance of each layer parameters on the GRG discrepancy can be investigated via multiple linear regression (MLR). Moreover, MLR is utilized to extract the objective function that relates the eight input layer parameters and the computed GRG for each individual row. Hence, the linear regression model that describes the relationship between eight independent inputs and a single dependable output can be formulated as:

$$y = r_0 + r_1a + r_2b + r_3c + r_4d + r_5e + r_6f + r_7g + r_8h + \in \quad (5)$$

for which a, b, c, d, e, f, g and h stand for the input layer parameters, r_0 is the intercept, $r_1r_2r_3r_4r_5r_6r_7r_8$ are the regression coefficients for the respective layer parameters and $\in$ is the error term. The error term ($\in$) is neglected when estimating the regression coefficients in which the objective function is finally expressed as:

$$y' = r_0 + r_1a + r_2b + r_3c + r_4d + r_5e + r_6f + r_7g + r_8h \quad (6)$$

The objective function is then evaluated using the grey wolf optimizer (GWO) algorithm in which the leadership hierarchy and hunting mechanism of the grey wolf in nature are emulated. The GWO algorithm is a metaheuristic optimization algorithm inspired by the social hierarchy and hunting behavior of grey wolves. It was proposed by Mirjalili et al. [30] in 2014. The algorithm mimics the hunting mechanism of grey wolves in the wild, where they follow three main roles: alpha, beta, and delta wolves [31].

However, in this work, the leadership hierarchy of the grey wolf is emulated by categorizing the initial population into four different groups namely as alpha (α), beta (β), delta (δ) and omega (ω). The α acts as the leader of a pack of wolves allocated at the first level in the hierarchy. The β is subordinated to α that might provide assistance in making decisions and activities of the pack. The δ is subordinated to the β and the ω is the lowest ranking of the hierarchy. Although the δ hierarchically dominates the ω, both still must submit to the α and ω.

The GWO algorithm is basically based on the mathematical modeling of the hunting approaches and social behaviors of the grey wolves. Figure 3 shows the

pseudo code of the GWO algorithm where k represents the current iteration, s is a parameter which linearly decreased from 2 to 0 over the course of iterations, A and C are coefficient vectors, X_α X_β and X_δ are the position vectors of grey wolves.

initialize the grey wolves population $X_i(i = 1,2,....,n)$
initialize α, A *and* C
compute the fitness of search agent
X_α = *the best search agent*
X_β = *the second best search agent*
X_δ = *the third best search agent*
While (k<maximum number of iterations)
for each search agent
update the position of the current search agent
end for
update s, A and C
compute the fitness of all search agents
update X_α X_β *and* X_δ
$s=s+1$
end while
return X_α

Fig. 3. Pseudo code of the GWO algorithm.

Since the primary aim of this research work is to search the maximum magnitude of the objective function, it is then inverted and formulated within the pre-specified lower and upper boundaries. Thus, the main preferences for the GWO algorithm applied in this work are shown as follows:

Population size of grey wolves = 300
Max. no. of iterations = 100
No. of input variables = 8
Minimize -f(*GRG*)
Subject to the constraints:
$0.1\ \mu m \leq a \leq 0.9\ \mu m$
$0.5\times10^{18}\ cm^{-3} \leq b \leq 9.5\times10^{18}\ cm^{-3}$
$0.1\ \mu m \leq c \leq 0.9\ \mu m$
$0.5\times10^{18}\ cm^{-3} \leq d \leq 9.5\times10^{18}\ cm^{-3}$
$0.1\ \mu m \leq e \leq 0.9\ \mu m$
$0.5\times10^{13}\ cm^{-3} \leq f \leq 9.5\times10^{13}\ cm^{-3}$
$0.1\ \mu m \leq g \leq 0.9\ \mu m$
$0.5\times10^{17}\ cm^{-3} \leq h \leq 9.5\times10^{17}\ cm^{-3}$

3. Results and Discussion

This section comprehensively discusses the overall results of the metaheuristic modelling of multiple layer parameter devices SC device. Data manipulation is conducted by employing GRA in order to ease the modelling complexity. Table 4 comprises the computed magnitudes of deviation sequences, GRCs and GRGs based on L27 OA Taguchi-based DoE.

Table 4. Computed magnitudes of deviation sequences, GRCs and GRGs.

Exp. No.	Deviation Sequences, Δ_{oi} *(n)*		*GRC (n)*		*GRG (n)*	Rank
	J_{sc}	PCE	J_{sc}	PCE		
1	0.9988	1	0.3336	0.333333	0.333467	27
2	0.947187	0.209738	0.345498	0.704485	0.524992	13
3	0.932333	0	0.349081	1	0.67454	2
4	0.985446	0.692884	0.336599	0.419152	0.377876	23
5	0.945986	0.153558	0.345785	0.765043	0.555414	9
6	0.932933	0.136704	0.348935	0.785294	0.567114	8
7	0.983496	0.625468	0.337042	0.44426	0.390651	20
8	0.947487	0.314607	0.345426	0.613793	0.47961	17
9	0.934584	0.054307	0.348533	0.902027	0.62528	6
10	0.983946	0.850187	0.336939	0.370319	0.353629	25
11	0.947637	0.213483	0.34539	0.700787	0.523089	14
12	0.934434	0.022472	0.34857	0.956989	0.652779	3
13	0.984846	0.683521	0.336735	0.422468	0.379602	22
14	0.948687	0.308989	0.34514	0.618056	0.481598	16
15	0.936084	0.172285	0.348169	0.743733	0.545951	11
16	1	0.838951	0.333333	0.373427	0.35338	26
17	0.948687	0.335206	0.34514	0.598655	0.471897	19
18	0.933683	0.044944	0.348752	0.917526	0.633139	4
19	0.984546	0.833333	0.336803	0.375	0.355902	24
20	0.949587	0.235955	0.344926	0.679389	0.512158	15
21	0.936834	0.052434	0.347987	0.905085	0.626536	5
22	0	0.891386	1	0.359354	0.679677	1
23	0.949137	0.194757	0.345033	0.719677	0.532355	12
24	0.934584	0.157303	0.348533	0.760684	0.554608	10
25	0.987547	0.677903	0.336124	0.424483	0.380304	21
26	0.948387	0.327715	0.345212	0.604072	0.474642	18
27	0.935034	0.061798	0.348424	0.89	0.619212	7

The rank of GRGs is evaluated based on their higher order of magnitude. The quality of multiple responses (J_{sc} and PCE) is portrayed by the magnitude of calculated GRG in each row. In this case, experimental row no. 22nd exhibits the highest calculated GRG, implying that the combinational layer parameters employed in row no. 22nd would produce the optimal J_{sc} and *PCE* magnitudes.

Applying the MLR approach with aim of modeling the regression equation is a crucial step in linking the correlation between multiple layer parameters and the GRG. Forming up a correlation between the calculated GRGs and the layer parameters such as SnO_2:F thickness, SnO_2:F donor density, WS_2 thickness, WS_2 donor density, $CH_3NH_3PbI_3$ thickness, $CH_3NH_3PbI_3$ donor density, MoS_2 thickness and MoS_2 acceptor density is essential in formulating the objective function. The correlation between eight input layer parameters and the GRGs is statistically described in normal Q-Q plot (Fig. 4). The results of the MLR analysis are summarized in Table 5.

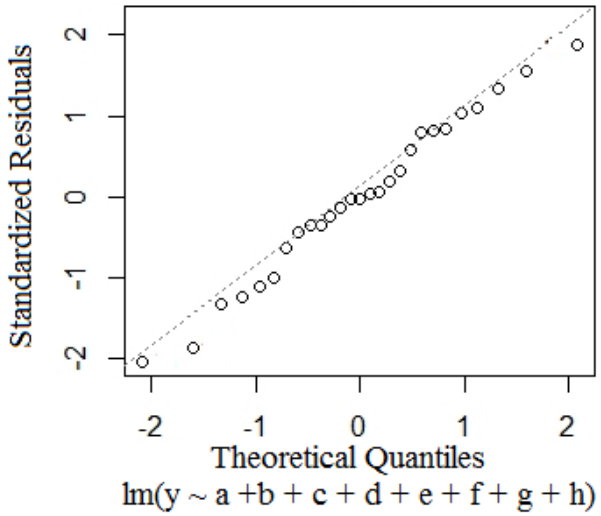

Fig. 4. Normal Q-Q for eight layer parameters.

Table 5. Summary of MLR Analysis.

Term	Regression Coefficients	Std. Error	t value	Pr (>|t|)	Signif. code
Intercept	0.262084	0.064622	4.056	0.000742	***
a	0.038231	0.050733	0.754	0.460843	
b	-0.001791	0.003805	-0.471	0.643442	
c	-0.066809	0.050733	-1.317	0.204398	
d	0.005241	0.003805	1.377	0.185250	
e	0.350866	0.050733	6.916	1.83e-06	***
f	0.004255	0.003805	1.118	0.278113	
g	0.017364	0.050733	0.342	0.736114	
h	0.007094	0.003805	1.864	0.078673	
Significant Code: 0 '*', 0.001 '**', 0.01 '*', 0.05 '.' 0.1-1 ' '**					
Residual standard error: 0.06457 on 18 degrees of freedom					
Multiple R-squared: 0.7603, Adjusted R-squared: 0.6538					
F-statistic: 7.137 on 8 and 18 DF, p-value: 0.0002778					

Layer parameter e ($CH_3NH_3PbI_3$ thickness) is regarded as the most dominant factor influencing the GRGs with probability value (1.83e-06). Diversely, the rest of the layer parameters are regarded as neutral factors (probability value > 0.05) in which their magnitudes do not contribute much influence on the GRG. The developed MLR model in this work is mathematically formulated as:

$$f(GRG) = 0.262084 + 0.038231*a - 0.001791*b - 0.066809*c + 0.005241*d + 0.350866*e + 0.004255*f + 0.017364*g + 0.00709*h \quad (7)$$

The model is then inverted within the specified upper and lower boundaries in order to fit into GWO algorithm for solving the maximization problem. Therefore, the objective function of the maximization problem for GWO algorithm can be mathematically written as:

$$f(GRG)^{-1} = -0.262084 - 0.038231*a + 0.001791*b + 0.066809*c - 0.005241*d - 0.350866*e - 0.004255*f - 0.017364*g - 0.00709*h \quad (8)$$

The GWO algorithms are implemented using MATLAB software. After 100^{th} iterations, the minimum magnitude of the inverted objective function is converged at -0.7531 as depicted in Fig. 5. The optimum layer parameters yielding the most minimum magnitude of the objective function are predicted as; SnO_2:F thickness (0.614 µm), SnO_2:F density (0.5×10^{18} cm^{-3}), WS_2 thickness (0.1 µm), WS_2 donor density (9.5×10^{18} cm^{-3}), $CH_3NH_3PbI_3$ thickness (0.9 µm), $CH_3NH_3PbI_3$ donor density (9.5×10^{13} cm^{-3}), MoS_2 thickness (0.1 µm) and MoS_2 acceptor density (9.5×10^{17} cm^{-3}).

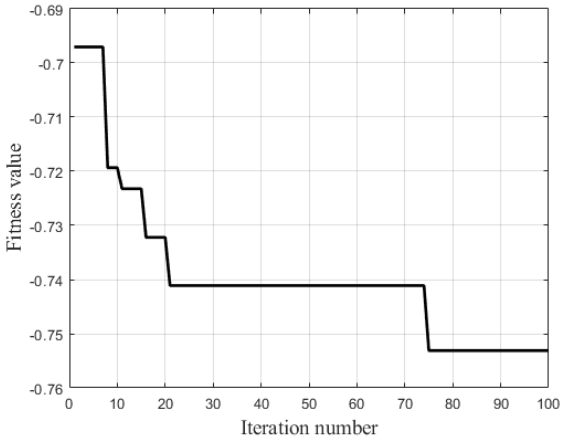

Fig. 5. Convergence plot of GWO.

To verify the predictive performance of the proposed metaheuristic approach, the PSC device is re-simulated using the predicted layer parameters. The band of energy in a PSC represents the energy states of electrons and is fundamental for converting sunlight into electrical power. PSCs rely on multiple energy levels, typically showing the p-type and n-type region which is halved by intersection. Implanting process in p-type PSCs leads to an excess of positively charged "holes," where the valence band is nearly proximate to the Fermi level. In n-type PSC, doping results in more negatively charged electrons, forcing the conduction band proximate to the Fermi level. The meeting point forms a depletion layer without free carriers and creates an electric field. Photons striking the solar cell excite electrons, generating electron-hole pairs. Figure 6 depicts the energy band diagram of the optimized PSC configuration.

The disparity in lattice parameters at interfaces induces defects, which promote exciton recombination. At these interfaces, two types of band alignments, known as cliff and spike structures, can arise, often facilitating charge carrier recombination. The cliff structure specifically causes bending of the conduction band, while achieving optimal efficiency at the p-n junction requires a positive band offset—akin to the spike structure. In the optimized PSC design, the positive spike offset measures +0.33 eV (refer to Fig. 6), indicating enhanced device performance due to effective band alignment. This improvement is associated with the absorber layer ($CH_3NH_3PbI_3$) recombination activation energy (E_a), which is crucial for device functionality.

Within the depletion region, the electric field separates excitons (electrons and holes), producing current upon connection to an external circuit [32]. The band diagram illustrates electron energy states and shows how absorbed photons elevate electrons from the valence to conduction bands, thereby generating electrical current [32]. In the optimized PSC, the band alignment shifts subtly, with the band gap narrowing progressively with distance, a result of band bending at the interfaces.

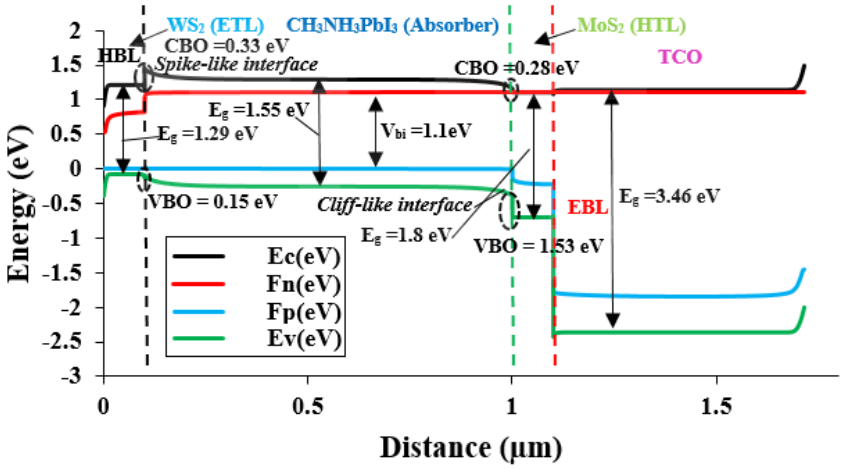

Fig. 6. Energy band diagram of the optimized PSC configuration.

The band structure reveals a built-in voltage gap of approximately +1.1 eV, with potential variations caused by band bending across various interfaces. The built-in voltage (V_{bi}), which represents the potential difference between the valence band of a p-type semiconductor and the conduction band of an n-type semiconductor, measures 1.1 eV at 300K under thermal equilibrium. In this state, electron flow is steady at a constant temperature. As temperature rises, lattice vibrations increase, which can lead to a reduction in the semiconductor's bandgap (E_g), or the energy separation between the valence and conduction bands.

With a narrowed bandgap, the energy gap between the Fermi levels (Fp for p-type and Fn for n-type) decreases, leading to a reduced V_{bi} within the PSC structure. In the energy diagram, MoS_2's LUMO level acts as the electron-blocking layer (EBL) at 3.46 eV, while in the $CH_3NH_3PbI_3$ region, the valence band edge is at 1.29 eV, and the conduction band edge at 1.8 eV. The HOMO level of WS_2 functions as the hole-blocking layer (HBL) at 1.55 eV, with these energy levels and temperature effects influencing PSC performance.

An interface resembling a "cliff" emerges between $CH_3NH_3PbI_3$ and MoS_2, where the conduction band offset (CBO) of +0.28 eV forms an electron-blocking barrier from the absorber layer toward the hole transport layer (HTL). This barrier is unfavourable as it increases charge carrier recombination, thus lowering the device's efficiency by permitting electron backflow across the junction. In a similar way, a cliff interface between $CH_3NH_3PbI_3$ and WS_2 shows a valence band offset (VBO) of -0.15 eV, leading to a potential drop that restricts hole movement from the absorber to the electron transport layer (ETL). Such cliff interfaces can lead to hole accumulation, raising recombination rates. The VBO at the $WS_2/CH_3NH_3PbI_3$

boundary measures 0.15 eV, creating a minor barrier, whereas the $MoS_2/CH_3NH_3PbI_3$ interface displays a larger barrier of 1.53 eV, posing a substantial restriction for hole transfer. Meanwhile, the CBO at the $WS_2/CH_3NH_3PbI_3$ interface is 0.33 eV, forming a strong electron barrier, while that at the MoS_2 interface is slightly lower at 0.28 eV, creating a lesser obstacle.

Modifying the voltage in PSCs has a pronounced effect on capacitance, directly impacting the cell's charge storage capability. In PSCs, capacitance is inherently tied to the electronic properties of the materials used. Shifts in voltage affect energy states, adjust the Fermi level, and modify the concentration of charge carriers, all of which alter capacitance. Furthermore, temperature has a significant influence on the dielectric properties, leading to increased capacitance. This temperature impact on solar cell performance can be assessed through Mott-Schottky (MS) analysis, represented by specific measurements denoted as.

$$\frac{1}{C^2} = \frac{1}{S^2.\varepsilon.q} \times \frac{1}{N_a} \times \left(V - V_{bi} - \frac{k_b T}{q}\right) \quad (9)$$

In this case, C corresponds to capacitance, S to surface area, q to the elementary charge, and ε to the space permittivity. N_a indicates the acceptor density, V_{bi} refers to the built-in voltage (flat band potential), kB is the Boltzmann constant, and T stands for temperature in Kelvin units. As shown in Fig. 7(a), low bias below 0.5 V has no effect on capacitance, while a higher bias above 0.5 V alters the capacitance. The V_{bi} is determined at the point where the tangent line meets the voltage axis on the MS plots, as illustrated in Fig. 7 (b). In Fig. 7(b), at 300 K, the V_{bi} registers at +1.1 eV, corresponding with the band diagram shown in Fig. 6 for the same temperature.

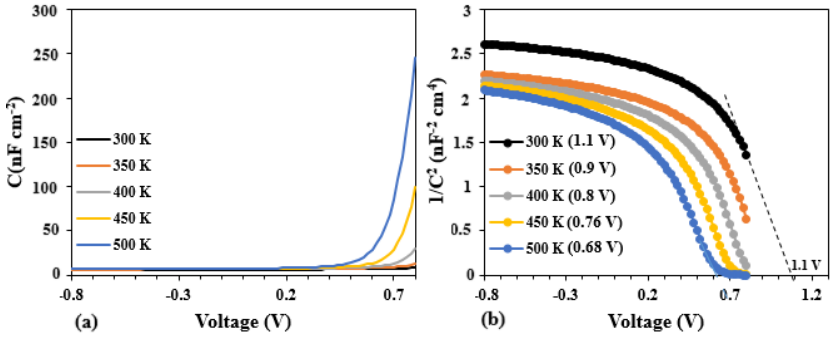

Fig. 7. (a) The impact of voltage on capacitance and (b) Mott-Schottky (MS) analysis.

This result indicates that the band alignment in the optimized PSC design is stable. However, as the temperature rises from 300 K to 500 K, the V_{bi} decreases from +1.1 eV to +0.68 V, pointing to increased exciton recombination likely due to higher series resistance. The PSC design maintains an efficiency of 82% at 350 K, though efficiency declines to approximately 62% at 500 K due to substantial recombination losses. The V_{bi} arises due to the potential difference established at equilibrium between the p-type and n-type regions of a p-n junction, caused by the movement of charges.

At first, the diffusion of majority carriers creates zones of opposite charges, forming a depletion region that determines V_{bi}. Changes in temperature can affect carrier density and the width of the depletion region, impacting V_{bi}. The alignment of energy bands across the junction controls how current flows through the device. Voltage fluctuations alter charge carrier movement, field strength, and material properties, impacting charge storage and the overall efficiency and stability of PSC devices. A thorough grasp of the generation and recombination behaviors of a PSC requires knowledge of fundamental principles. Charge carriers are generated when photons are absorbed, provided their energy is equal to or exceeds the material's bandgap energy (E_g), allowing electron-hole pairs to be created [33]. Materials with higher absorption coefficients (α) enhance photon uptake, leading to increased production of charge carriers [34], as illustrated in Eq. (10).

$$G = \propto . \Phi \tag{10}$$

The photon flux and generation process are symbolized by Φ and G, respectively. The recombination of electrons and holes results in the emission of a photon, particularly in materials with a direct bandgap. The energy produced from this recombination is given to a different charge carrier. SRH recombination, significant in defective materials, happens through defect states within the bandgap [35]. The rate of this recombination is defined by Eq. (11).

$$R_{SRH} = \frac{nP - n_i^2}{\tau_{p(n+n_i)+(P+n_i)}} \tag{11}$$

Carrier lifetimes are denoted by τ_p and τ_n, and n_i refers to the inherent concentration of charge carriers. When in a state of equilibrium, the rates of generation and recombination processes are identical, as shown in Eq. (12).

$$G = R \tag{12}$$

Light exposure raises the rate of generation, creating additional electron-hole pairs and disrupting the balance. Consequently, this results in an increase in photocurrent; however, recombination decreases the open-circuit voltage (V_{oc}) by diminishing the number of available carriers. Elevated rates of recombination reduce the overall carrier count which decreases V_{oc}. Quantum efficiency (QE) gauges the effectiveness of photon absorption in generating carriers, and excessive recombination weakens QE by limiting carrier collection. Surface passivation, through reducing defects and passivating dangling bonds, decreases SRH recombination events [36].

The rates of carrier generation and recombination influenced by optical excitation. In the design of the perovskite solar cell (PSC), light enters through the electron transport layer (ETL), where the rates of exciton generation and recombination are lower than those on the hole transport layer (HTL) side within the absorbing layer. Figure 8 indicates that the generation rate exceeds the recombination rate, which enhances the operational efficiency of the cell and results in more consistent electrical performance.

An increased surface area allows for better light absorption without substantially increasing recombination, thereby improving the device's overall performance. The PSC's efficiency hinges on optimizing both the generation and recombination processes. By selecting superior materials and refining structural design to enhance electron-hole pair generation while minimizing recombination

through defect passivation, the power conversion efficiency (PCE) can be improved. This interplay is more clearly illustrated by examining the right and left axes of Fig. 8. The comparison of *J-V* transfer curves between the pre-metaheuristic and post-metaheuristic are depicted in Fig. 9.

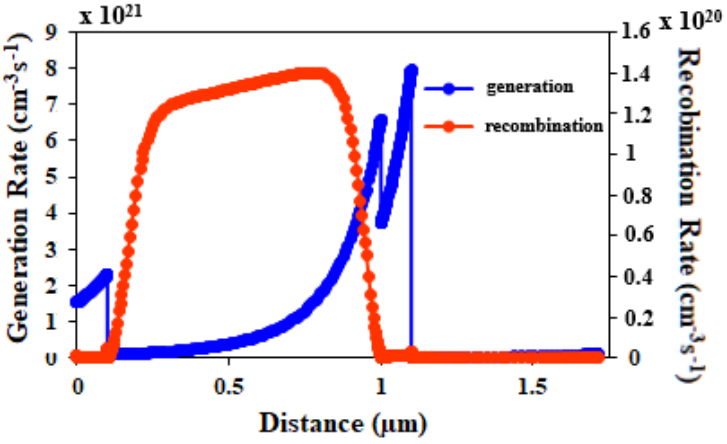

Fig. 8. Generation -recombination characteristics.

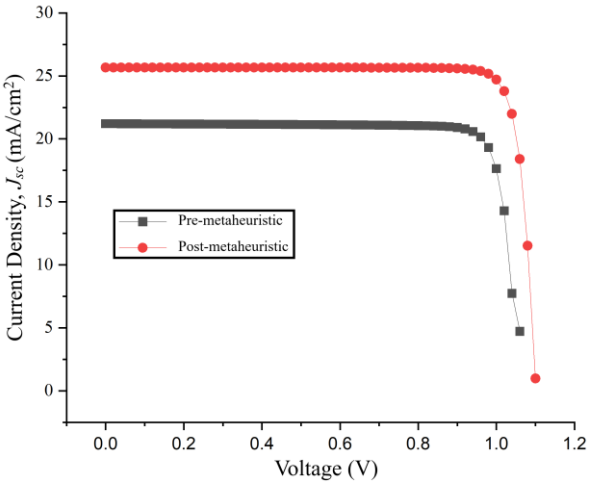

Fig. 9. J-V transfer curves of PSC device during pre-metaheuristic and post-metaheuristic optimization.

Based on the graph, the J_{sc} of the PSC device has improved by ~17.4% after going through metaheuristic modeling. The J_{sc} magnitude of the PSC device after metaheuristic modeling has increased to 25.67 mA/cm^2. Figure 10 shows the cylindrical graph indicating the improvement of both J_{sc} and *PCE* of the PSC device during pre-metaheuristic and post-metaheuristic. The *PCE* of the PSC device has been observed to have a decent improvement after the metaheuristic modeling where the *PCE* has improved to 24.73% compared to 19.38% (pre-metaheuristic). There is a decent increase of 5.35% in *PCE* magnitude.

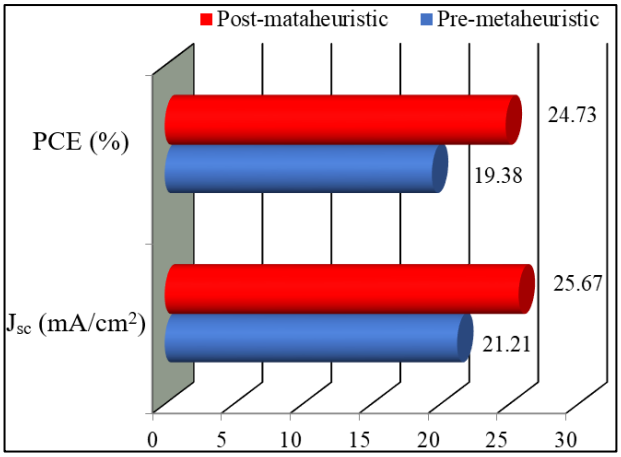

Fig. 10. Comparative cylindrical graph of J_{sc} and *PCE* between pre-metaheuristic and post-metaheuristic.

Based on the previous variance analysis, the MoS_2 (HTL) acceptor density has been identified as the most dominant factor influencing both J_{sc} and *PCE* magnitude. The acceptor concentration of MoS_2 plays a crucial role in enhancing J_{sc} and *PCE* as a suitably higher-level density (9.5×10^{17} cm^{-3}) is applied as previously predicted by metaheuristic approach. The scattering event occurred in the MoS_2 layer at lower doping density does affect the hole mobility.

As temperature increases deliberately, the effects of scattering significantly reduce the hole mobility. Hence, increasing the acceptor density of the MoS_2 layer would subsequently increase the probability of carrier's collision where the hole mobility is tremendously boosted as well as total current density. Higher generated J_{sc} may definitely contribute a significant impact on achieving better *PCE* as the ratio of energy output from the PSC device to input energy from the sun becoming much higher. Table 6 summarizes the optimized magnitudes of the layer parameters as compared to pre-metaheuristic.

Table 6. Summary of Optimized Parameters of the PSC device.

Input/output Parameter	Units	Pre-metaheuristic	Post-metaheuristic
SnO_2:F thickness	µm	0.2	0.614
SnO_2:F donor density	cm^{-3}	1×10^{18}	0.5×10^{18}
WS_2 thickness	µm	0.2	0.1
WS_2 donor density	cm^{-3}	1×10^{18}	9.5×10^{18}
$CH_3NH_3PbI_3$ thickness	µm	0.2	0.9
$CH_3NH_3PbI_3$ donor density	cm^{-3}	1×10^{13}	9.5×10^{13}
MoS_2 thickness	µm	0.2	0.1
MoS_2 acceptor density	cm^{-3}	1×10^{17}	9.5×10^{17}
Power conversion efficiency (PCE)	%	19.38	24.73
Current Density (J_{sc})	A/cm^2	21.21×10^{-3}	25.67×10^{-3}

It can be concluded that the proposed metaheuristic approach involving multiple methods such as L_{27} OA Taguchi-based DoE, GRA, MLR and GWO has been successfully modeling multiple layer parameters of the PSC device for much

improved J_{sc} and *PCE*. The proposed predictive approach is capable of estimating the most optimal value of layer parameters within the specified/desired lower and upper boundaries for higher J_{sc} and *PCE* of the PSC device.

4. Conclusions

Multiple layer parameters of the PSC device have been predictively modeled through a metaheuristic approach combining simulation tool (SCAPS), L_{27} OA Taguchi-based DoE, GRA, MLR and GWO. The output data are retrieved via SCAPS simulation guided by L_{27} OA Taguchi-based DoE. The output data (J_{sc} and *PCE*) are then manipulated to be a single representative unit by using GRA purposely for much easier computation. The MLR analysis is subsequently conducted in order to develop the objective function that relates multiple input layer parameters to the GRG variations. From the analysis, $CH_3NH_3PbI_3$ thickness is identified as the most dominant layer parameter influencing the GRG. Since the GWO algorithms are specifically developed to search for the minimum value of the objective function, the objective function has to be inverted (for searching the maximum point). After 100^{th} iterations, the minimum magnitude of the inverted objective function is converged at -0.7531.

The final results reveal that the metaheuristic approach has successfully predicted the most optimal value of layer parameters within the specified/desired lower and upper boundaries where both J_{sc} and *PCE* of the PSC device are optimized to 25.67 mA/cm^2 and 24.73%, respectively. Future research could examine and integrate alternative computational intelligence methods beyond the GWO algorithm with Taguchi-GRA for more precise and thorough outcomes. These important discoveries showcase the advancements made in modeling PSC structures. Ultimately, the results of this work can guide future efforts in developing highly efficient PSCs.

Acknowledgement

The authors would like to thank the Ministry of Higher Education (MOHE) for sponsoring this work under project (FRGS/1/2024/TK07/UTEM/03/4) and MiNE, CeTRI, Faculty of Electronic and Computer Technology and Engineering (FTKEK), Universiti Teknikal Malaysia Melaka (UTeM) for the moral support throughout the project. The authors would also like to thank Dr. Marc Burgelman of the University of Gent in Belgium for supplying the SCAPS-1D simulation program.

Nomenclatures

A	A coefficient vector
C	A coefficient vector
E_g	Bandgap Energy
E_r	Relative Permittivity
J_{sc}	Short Circuit Current Density
N_a	Acceptor Density
N_c	Conduction Band Density
N_d	Donor Density
N_t	Defect Density
s	A parameter which linearly decreased from 2 to 0 over the course of iterations

X_α	Best Search Agent
X_β	Second Best Search Agent
X_δ	Third Best Search Agent
$\hat{Z}_0$	Normalizing larger-the-better objective problem
$Z_o(n)$	Output parameters of the PSC device (J_{sc} and PCE)

Greek Symbols

α	Alpha
β	Beta
δ	Delta
ω	Omega
ε	Distinguishing Coefficient
ϵ	Error term
μ_n	Electron Mobility
μ_p	Hole Mobility
χ	Electron Affinity

Abbreviations

CIGS	Copper Indium Gallium Selenide Solar Cell
CBO	Conduction Band Offset
CdS	Cadmium Sulfide
$CH_3NH_3PbI_3$	Methylammonium Lead Iodide
CuTe	Copper Telluride
DoE	Design of Experiments
DSSC	Dye-sensitized Solar Cell
EBL	Electron Blocking Layer
ETL	Electron Transport Layer
FF	Fill Factor
GRA	Grey Relational Analysis
GRC	Grey Relational Coefficient
GRG	Grey Relational Grade
GWO	Grey Wolf Optimizer
HBL	Hole Blocking Layer
HTL	Hole Transport Layer
HOMO	Highest Occupied Molecular Orbital
LUMO	Lowest Unoccupied Molecular Orbital
MLR	Multiple Linear Regression
MoS_2	Molybdenum Disulfide
OA	Orthogonal Array
PCE	Power Conversion Efficiency
PSC	Perovskite Solar Cell
PV	Photovoltaic
RSM	Response Surface Methodology
SCAPS	Solar Cell Capacitance Simulator
SnO_2:F	Spray Pyrolyzed Fluorine-Doped Tin Oxide
SRH	Shockley-Read-Hall Recombination
TCO	Transparent Conducting Oxide
VBO	Valance Band Offset
WS_2	Tungsten Disulfide

References

1. Ghosh, S.; Yasmin, S.; Ferdous, J.; and Saha, B.B. (2022). Numerical analysis of a CZTS solar cell with MoS_2 as a buffer layer and graphene as a transparent conducting oxide layer for enhanced cell performance. *Micromachines*, 13(8), 1-14.
2. Roy, P.; Ghosh, A.; Barclay, F.; Khare, A.; and Cuce, E. (2022). Perovskite solar cells: A review of the recent advances. *Coatings*, 12(8), 1-24.
3. Mehtab-Ur-Rehman.; and Wang Qun. (2023). The organic-inorganic solar cells device structure with different transport layers and compounds: The guidelines for researchers. *World Journal of Advanced Research and Reviews*, 17(1), 846-855.
4. Touafek, N.; Mahamdi, R.; and Dridi, C. (2021). Boosting the performance of planar inverted perovskite solar cells employing graphene oxide as HTL. *Digest Journal of Nanomaterials and Biostructures*, 16(2), 705-712.
5. Alla, M. et al. (2022). Optimized $CH_3NH_3PbI_3$-XClX based perovskite solar cell with theoretical efficiency exceeding 30%. *Optical Materials*, 124, 112044.
6. Devi, V.L.; Kuchhal, P.; De, D.; Sharma, A.; Shukla, N.K.; and Aggarwal, M. (2024). Machine learning-driven optimization of transport layers in MAPbI3 perovskite solar cells for enhanced performance. *IEEE Access*, 12, 179546-179565.
7. Khan, T.M.; Saidani, O.; and Al Ahmed, S.R. (2024). Utilizing machine learning to enhance performance of thin-film solar cells based on Sb 2 (SxSe1−x) 3: Investigating the influence of material properties. *RSC Advances*, 14(38), 27749-27763.
8. Chabane, H. et al. (2024). Optimized Al0.25Ga0.75as solar cell performance using a new approach based on hybridizing Silvaco TCAD simulator with real coded genetic algorithm. *Journal of Optics*, 1-16.
9. Makableh, Y.F.; Alzubi, H.; and Tashtoush, G. (2021). Design and optimization of the antireflective coating properties of silicon solar cells by using response surface methodology. *Coatings*, 11(6), 1-13.
10. Mohammed, A.R.; and Fahim, I.S. (2020). Tandem organic solar cell optimization using response surface methodology. *Proceedings of the International Conference on Data Analytics for Business and Industry: Way Towards a Sustainable Economy* (*ICDABI*), Sakheer, Bahrain.
11. Bahrudin, M.S. et al. (2018). Jsc and Voc Optimization of perovskite solar cell with interface defect layer using Taguchi method. Proceedings of the *IEEE International Conference on Semiconductor Electronics* (*ICSE*), Kuala Lumpur, Malaysia.
12. Zapata-Cruz, J.R. et al. (2019). Implementation of Taguchi method to investigate the effect of electrophoretic deposition parameters of SnO_2 on dye sensitised solar cell performance. *Materials Technology*, 34(9), 549-557.
13. Bahrudin, M.S.; Yusoff, Y.; Abdullah, S.F.; Zuhdi, A.W.M.; Amin, N.; and Ahmad, I. (2020). An innovative parametric optimization using Taguchi method for Cu(In,Ga)(S,Se)2 thin film solar cell device simulation. *Journal of Energy and Environment*, 12(2), 1-7.

14. Olabi, A.G. et al. (2023). Optimal parameter identification of perovskite solar cells using modified bald eagle search optimization algorithm. *Energies*, 16(1), 1-15.
15. Hunde, B.R.; and Woldeyohannes, A.D. (2023). Performance analysis and optimization of perovskite solar cell using SCAPS-1D and genetic algorithm. *Materials Today Communications*, 34. 105420.
16. Kaharudin, K.E. et al. (2023). Predictive analytics of junctionless double gate strained MOSFET using genetic algorithm with DoE-based grey relational analysis. *Journal of Engineering Science and Technology*, 18(6), 3077-3096.
17. Kaharudin, K.E.; Salehuddin, F.; Zain, A.S.M.; and Roslan, A.F. (2020). Predictive analytics of CIGS solar cell using a combinational GRA-MLR-GA model. *Journal of Engineering Science and Technology*, 15(4), 2823-2840.
18. Kaharudin, K.E.; and Salehuddin, F. (2022). Predictive modeling of mixed halide perovskite cell using hybrid L27 OA Taguchi-based GRA-MLR-GA approach. *Jurnal Teknologi*, 84(1), 1-9.
19. Kaharudin, K.E.; Salehuddin, F.; Zain, A.S.M.; and Aziz, M.N.I.A. (2017). Application of Taguchi-based grey fuzzy logic for simultaneous optimization in TiO2/WSix-based vertical double-gate MOSFET. *Journal of Telecommunication*, *Electronic and Computer Engineering*, 9(2-13), 23-28.
20. Kaharudin, K.E. et al. (2016). Design and optimization of TiSix/HfO2 channel vertical double gate NMOS device. *Proceedings of the IEEE International Conference on Semiconductor Electronics* (*ICSE*), Kuala Lumpur, Malaysia.
21. Oboh, I.O.; Offor, U.H.; and Okon, N.D. (2022). Artificial neural network modeling for potential performance enhancement of a planar perovskite solar cell with a novel TiO2/SnO2 electron transport bilayer using nonlinear programming. *Energy Reports*, 8, 973-988.
22. Kohnehpoushi, S.; Nazari, P.; and Nejand, B.A. (2018). MoS2 : A two-dimensional hole-transporting material for high-efficiency, low-cost perovskite solar cells. *Nanotechnology*, 29(20), 1-8.
23. Sobayel, K. et al. (2019). A comprehensive defect study of tungsten disulfide (WS2) as electron transport layer in perovskite solar cells by numerical simulation. *Results in Physics*, 12, 1097-1103.
24. Burgelman, M.; Decock, K.; Kheli, S.; and Abass, A. (2013). Advanced electrical simulation of thin film solar cells. *Thin Solid Films*, 535, 296-301.
25. Soro, D. et al. (2022). Simulation of a CIGS solar cell with CIGSe2/MoSe2/Mo rear contact using AFORS-HET digital simulation software. *Modeling and Numerical Simulation of Material Science*, 12(2), 13-23.
26. Teuou Ngoupo, A.; and Ndjanka, J.M.B. (2022). Performance enhancement of Sb2Se3-based solar cell with hybrid buffer layer and MoSe2 as a hole transport material using simulator device. *Discover Mechanical Engineering*, 1(5), 1-18.
27. Haque, M.D.; Ali, M.H.; Rahman, M.F.; and Islam, A.Z.M.T. (2022). Numerical analysis for the efficiency enhancement of MoS2 solar cell: A simulation approach by SCAP-1D. *Optical Materials*, 131, 112678.
28. He, X.; Iwamoto, Y.; Kaneko, T.; and Kato, T. (2022). Fabrication of near-invisible solar cell with monolayer WS2. *Scientific Reports*, 12(1), 1-8.

29. Ju-Long, D. (1982). Control problems of grey systems. *Systems and Control Letters*, 1(5), 288-294.
30. Mirjalili, S.; Mirjalili, S.M.; and Lewis, A. (2014). Grey wolf optimizer. *Advances in Engineering Software*, 69, 46-61.
31. Nadimi-Shahraki, M.H.; Zamani, H.; Asghari Varzaneh, Z.; Sadiq, A.S.; and Mirjalili, S. (2024). A systematic review of applying grey wolf optimizer, its variants, and its developments in different Internet of Things applications. *Internet of Things*, 26, 101135.
32. Njema, G.G.; Kibet, J.K.; and Ngari, S.M. (2025). Performance optimization of a novel perovskite solar cell with power conversion efficiency exceeding 37% based on methylammonium tin iodide. *Next Energy*, 6, 100182.
33. Sabri, S.; Malek, R.; and Kassmi, K. (2023). Improvement efficiency of solar cells using III-V Dual Junction: InGaP/GaAs. *Key Engineering Materials*, 954, 97-109.
34. Arunachalam, J.; and Sivaperuman, K. (2024). An investigation of the influence of various factors on the electrical performance of a ($CuGaS_2$) -based thin-film solar cell using SCAPS-1D software. *Optik*, 303, 171744.
35. Vedel, C.D.; Gunst, T.; Smidstrup, S.; and Georgiev, V.P. (2023). Shockley-Read-Hall recombination and trap levels in In0.53Ga0.47As point defects from first principles, *Physical Review B*, 108(9), 1-9.
36. Min, J.; Choi, Y.; Kim, D.; and Park, T. (2024). Beyond imperfections: exploring defects for breakthroughs in perovskite solar cell research. *Advanced Energy Materials*, 14(6), 2302659.